Detecting Displacements Within Archaeological Sites in Cyprus After a 5.6 Magnitude Scale Earthquake Event Through the Hybrid Pluggable Processing Pipeline (HyP3) Cloud-Based System and Sentinel-1 Interferometric Synthetic Aperture Radar (InSAR) Analysis

Athos Agapiou and Vasiliki Lysandrou

***Abstract*—The distribution of free and open access radar satellite datasets, like those of Sentinel-1, has provided new opportunities for monitoring archaeological sites and monuments in a systematic way, and especially after earthquake events. While optical sensors are established in the scientific literature and radar sensors are lately introduced in the relevant literature, the role of satellite-driven ready products is still limited discussed. With the continuous improvement of remote sensing satellite data quality and accuracy, high-resolution data needs to be processed, while at the same time, this required high computational complexity. In respect to this, over the last years, various efforts have been made to support high-performance cloud-based processing, providing to the end-users ready products in a short time. This study presents the results from the exploitation of a relevant new cloud platform, namely the Hybrid Pluggable Processing Pipeline (HyP3) system that integrates GAMMA software, for detecting ground displacement within archaeological sites in Cyprus, after a 5.6 magnitude scale earthquake in 2015. Ascending and descending pairs of Sentinel-1 images, acquired before and after the event, were processed through the HyP3 platform, revealing small relative ground displacements in the area under study. The processing chain was performed in less than 1 h -per pair- on the HyP3 system, indicating that similar approaches could be beneficial in the future to support cultural heritage management of large areas.**

***Index Terms*—Cultural heritage, earthquakes, Hybrid Pluggable Processing Pipeline (HyP3), interferometric SAR (InSAR), deformation, Sentinel-1.**

Manuscript received August 14, 2020; revised September 24, 2020; accepted September 28, 2020. Date of publication October 1, 2020; date of current version October 16, 2020. This work is submitted under the NAVIGATOR Project. This work was supported by the Republic of Cyprus and the Structural Funds of the European Union in Cyprus under the Research and Innovation Foundation under Grant EXCELLENCE/0918/0052 (Copernicus Earth Observation Big Data for Cultural Heritage). The Centre is currently being upgraded through the H2020 Teaming Excelsior Project (www.excelsior2020.eu). *(Corresponding author: Athos Agapiou.)*

The authors are with the Department of Civil Engineering and Geomatics, Faculty of Engineering and Technology, Cyprus University of Technology and the Eratosthenes Centre of Excellence, Limassol 3036, Cyprus (e-mail: athos.agapiou@cut.ac.cy; vasiliki.lysandrou@cut.ac.cy).

Digital Object Identifier 10.1109/JSTARS.2020.3028272

I. Introduction

EARTH observation is well established in the literature for monitoring purposes of large areas [1], [2]. During the last decade, the significant advancements of space technology have triggered novel methodologies for monitoring areas of archaeological interest all around the world [3], [4].

For instance, recent studies [5]– [7] have shown that both optical and radar sensors can be used to detect looting activities in conflicted areas, as the case of Syria, while Tapete and Cigna [8] have demonstrated that satellite sensors can map not-widely known flooding events in the vicinity of archaeological sites. An overview of the role of earth observation of cultural heritage applications can be found in [9] and [10].

The use of freely distributed and open-access satellite datasets such as those of Sentinels-1 have been investigated in the recent past for monitoring natural hazards. Several studies exist in the literature, whereas these sensors, as well as other radar satellites, are used for a rapid response to natural hazards, providing a rapid damage mapping [11]–[13].

In [14], pairs of Sentinel-1 images have been used to study the deformation analysis in Mindanao, Philippines, after four strong earthquakes of magnitude $>$6.4 occurred successively in 2019, while high coherence Sentinel-1 images processing were implemented for dam monitoring in [15]. The use of Sentinel-1 blended with freely distributed image software analysis was proposed as a solution for monitoring archaeological sites [16]. In [17], radar high-resolution satellite images were able to detect small displacements over the Historical Center of Rome. An overview of the trends and the perspectives of the spaceborne synthetic-aperture radar (SAR) applications for archaeological research can be found in [5], while the importance of the Copernicus radar sensors for geohazard assessments in cultural heritage sites is highlighted in [18].

Notwithstanding the plethora of examples on the use of satellite data for monitoring microdeformations, still, the processing chain of the radar deformation requires in-depth knowledge

of the radar theory [19], [20] and hardware accessibility with the high-computational performance [21]. While several free software packages have been developed in the recent past and are currently available, these remain technically complex and can be challenging to use for nonexperts [22].

The latest can be nowadays realized as the technological trend is moving toward big-data cloud-platforms [23]–[25] that can provide in short time satellite-driven ready products. These platforms enable end-users to have access to high-performance cloud computers, initially for the radiometric and geometric calibration of the radar images, before the generation of interferograms and vertical displacements.

As earth observation may support in multiple ways the disaster risk management cycle intended for tangible cultural heritage—see more in [26]—the technological advancements—in terms of computational changes of satellite data processing—can radically change the traditional way of processing of the data, from the desktop analysis to cloud-based analysis.

Already the use of the Google Earth Engine (GEE) [27] has been presented in the literature for archaeological and heritage management studies [28]. In the light of the above, this article aims to highlight the growing significance toward the analysis ready data (ARD). Therefore, this study showcases an example of a relevant new cloud platform namely the Hybrid Pluggable Processing Pipeline (HyP3) cloud-based system [29], operated by the Alaska Satellite Facility (ASF) [30]. The platform is still limited presented in the relevant literature [31], while no studies for their use for heritage management can be found.

The current study is organized as follows: after a brief introduction on the HyP3 platform, some details regarding the earthquake event are given. Then, the satellite data and the overall methodology are presented, with a particular focus on areas with archaeological interest. Last comes the conclusion section, highlighting the benefits and drawbacks of the study.

II. HyP3 System

The HyP3 platform was used for the needs of the current study for archaeological monitoring sites against natural hazards (earthquakes), and discusses the usability of ARD for heritage management [31]. HyP3 is a cloud-based system provided by the ASF—one of the Distributed Active Archive Centers (DAACs) [32], which archives and distributes SAR data available to researchers of a variety of disciplines worldwide. It provides custom on-demand higher-level SAR processing for users [29].

The HyP3 system relies on core Amazon services such as Lambda, the simple notification service, relational database service, elastic compute cloud (EC2), simple storage service, and Elastic Beanstalk [29]. Currently, the HyP3 system runs on a beta version and provides a specific amount of processing for a user per month (one-time processing). The platform was recently expanded to process beyond the ALOS PALSAR data, the Sentinel-1 datasets, through an international agreement between ASF and the European Space Agency (ESA).

The HyP3 system allows users to request satellite data processing using several predefined algorithms. Data were initially selected through the Earth Data ASF cloud platform [32]. The HyP3 system automatically accesses the ASF cloud-based archive through the DAAC RESTful application programming interface and processes the data on Amazon's EC2. Final products are distributed through Amazon's S3 and are available for users to download [33].

The HyP3 platform currently runs a series of different processing chains such as Interferometric SAR (InSAR), radiometric terrain correction, and change detection. The processing of the radar images is based on either the Sentinel Toolbox [34] or GAMMA software [35]. The end-users also can define a series of processing options, however, no commands for changing the process or any other graphic interface is available. Therefore, in its current version (v. 1.2), the HyP3 platform implements the predefined steps of the Sentinel Toolbox and GAMMA software in the cloud services of Amazon.

III. Earthquake Event

Cyprus was affected by strong earthquakes, since antiquity [36], as it is located on a seismic zone on the margin of two tectonic plates, namely the *Anatolian* plate on the north and the *African* plate on the south, forming the so-called the "Cyprus arc." The Cyprus arc is in the collision between these two plates that meet on the southern part of Cyprus [37].

One the most significant earthquakes that hit Cyprus in the recent years was a 5.6 magnitude scale seismic event that took place on 15th April 2015, at 08:25 UTC, and it was strongly felt throughout the country.

As reported in the official website of the Cyprus Geological Survey Department [38], the earthquake was "*very strongly felt in the Pafos district, especially in the epicentral area. Strongly felt in the Lemesos district. Moderately felt in the Lefkosia district and lightly felt in the Larnaka and Ammochostos districts.*" The epicenter of the earthquake was estimated at 8 km NW of Paphos (34.8238°N, 32.3690°E) with a depth of 27.62 km. This earthquake remains the biggest in Cyprus—until today—from the launch of the Sentinel-1 sensors in 2014.

Fig. 1 presents the seismicity events registered for the last five (5) years in Cyprus, by the Cyprus Geological Survey Department. The earthquake event under study is evidenced within the yellow square in Fig. 1.

Several sources of uncertainty arise when calculating the deformation of the surface using the InSAR deformation analysis. One of these sources is related to the errors of the topographic model [39] (see Fig. 2).

The highest peak of the island is placed on Troodos mountain, while—with exception of the capital of the island, Lefkosia (Nicosia)—the rest of the major urban centers are placed on the coastline: starting from Pafos on the west, Lemesos (Limassol) on the south, Larnaca on the south-east, Ammochostos (Famagusta) on the east and Keryneia on the north (see Fig. 2).

The seismic network of Cyprus (operated by the Cyprus Geological Survey Department, which is the official provider for earthquake information of the country), includes six (6) seismic stations all over Cyprus, and provides values related to the peak ground acceleration (PGA), the peak ground velocity, and the peak ground displacement. In detail, the earthquake

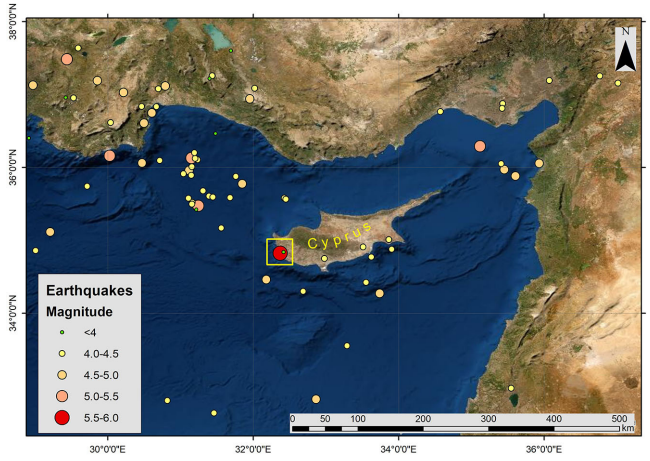

Fig. 1. Earthquake events in the wider area of Cyprus. The size of each event is relevant to the magnitude scale. Earthquake took place on 15th of April 2020 is shown within the yellow square circle. Data from the official website of the Cyprus Geological Survey Department. Map produced by Atho Agapiou.

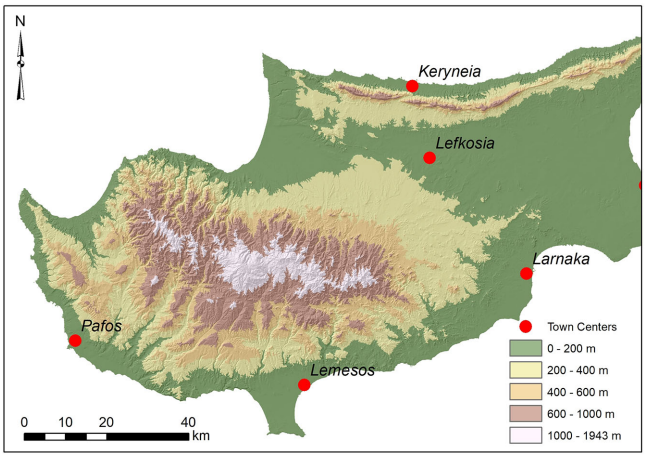

Fig. 2. Elevation zones of Cyprus and major towns of Cyprus. Map produced by Atho Agapiou.

was recorded from the HHE (East–West horizontal movements), HHN (North–South horizontal movements), and HHZ (vertical movements) channels. The results from this record are shown in Table I.

The *Akamas* station, located just some kilometers on the north of the epicenter of the earthquake has recorded significant displacements for all channels (HHZ = 0.07 m, HHN = 0.15 m, and HHZ = 0.16 m). Indeed, high displacement values in this area have been reported from the line of sight (LOS) wrapped interferogram, displacement fringes and vertical displacement of the ascending orbit. Smaller movements have also been reported from the rest of the stations that, however, are located further from the epicenter of the earthquake.

The differences between the vertical displacement and the ground stations should be linked with the reference point selected by the GAMMA processing chain. The products, therefore, can be assumed to provide relative differences from a reference point and these could be further elaborated with other ground measurements such as the global navigation satellite systems networks.

TABLE I
EARTHQUAKE EVET AS RECORDED FROM THE LOCAL SEISMIC NETWORK STATION OF THE CYPRUS GEOLOGICAL SURVEY DEPARTMENT

Station name	Channel	Peak Ground Acceleration (m/s^2)	Peak Ground Velocity (m/s)	Peak Ground Displacements (m)
Paralimni	HHZ	0.27	0.05	0.02
Paralimni	HHN	0.74	0.12	0.04
Paralimni	HHE	0.51	0.14	0.03
Mavrovouni	HHZ	0.29	0.03	0.01
Mavrovouni	HHN	0.39	0.04	0.02
Mavrovouni	HHE	0.39	0.07	0.01
Mathiatis	HHZ	0.56	0.08	0.02
Mathiatis	HHN	1.02	0.08	0.02
Mathiatis	HHE	0.71	0.07	0.02
Asgata	HHZ	1.13	0.06	0.02
Asgata	HHN	2.04	0.23	0.03
Asgata	HHE	1.81	0.13	0.02
Alefka	HHZ	4.78	0.33	0.05
Alefka	HHN	7.89	0.41	0.07
Alefka	HHE	8.58	0.57	0.07
Akamas	HHZ	9.75	0.54	0.07
Akamas	HHN	11.52	0.68	0.15
Akamas	HHE	12.06	0.77	0.16

HHE stands for East-West horizontal movements, HHN for North-South horizontal movements, and HHZ for vertical movements.

IV. DATA AND METHODOLOGY

A. Datasets

For the needs of the study, two pairs of Sentinel-1 images were used: one pair in ascending orbit (south pole toward the north pole) and the other pair in descending orbit (north pole toward the south pole). For each pair, an image before and after the event was used. In specific, the following two pairs of images in interferometric wide (IW) swath Single Look Complex (SLC)—were used: 1) a pair of images acquired on 14th April and 26th April 2015, in ascending mode; 2) a pair of images acquired on 15th April 2015 and 27th April 2015, with ascending mode. Table II summarizes the characteristics for the ascending orbit images and Table III the characteristics for the descending orbit images. It should be mentioned that in its current version, the HyP3 GAMMA InSAR processing supports only the VV polarization of the Sentinel-1 images [40].

B. Methodology

As mentioned earlier, the image processing chain applied for InSAR deformation analysis was executed through the HyP3 platform. In particular, the InSAR GAMMA algorithm was used. The methodology describing the GAMMA software for InSAR analysis using Sentinel images is comprised of 11 steps briefly described as follows [32].

Step 1: Determination of the overlapping area upon the Sentinel input images. At this stage, the imported images are cut in the overlap region such that only pixels (looks) from the same burst and subswath are combined into a multilook Intensity image.

Step 2: Download of an available digital elevation model (DEM) file, covering the overlap area. In our case study, the EU-DEM

TABLE II
ASCENDING SENTINEL-1 IMAGES' CHARACTERISTICS USED IN THE STUDY

Name	Characteristics
Date	14 April 2015 (15:49:11 UTC)
Instrument	SAR-C
Mode	Interferometric Wide swath (IW)
Satellite	Sentinel-1
Absolute Orbit number	5482
Pass direction	ASCENDING
Polarization	VV + VH
Product level	L1
Product type	Single Look Complex (SLC)
Path	160
Frame	109
Date	26 April 2015 (15:49:12 UTC)
Instrument	SAR-C
Mode	Interferometric Wide swath (IW)
Satellite	Sentinel-1
Absolute Orbit number	5657
Pass direction	ASCENDING
Polarization	VV + VH
Product level	L1
Product type	Single Look Complex (SLC)
Path	160
Frame	109

TABLE III
DESCENDING SENTINEL-1 IMAGES' CHARACTERISTICS USED IN THE STUDY

Name	Characteristics
Date	15 April 2015 (03:50:53 UTC)
Instrument	SAR-C
Mode	Interferometric Wide swath (IW)
Satellite	Sentinel-1
Absolute Orbit number	5489
Pass direction	DECENDING
Polarization	VV + VH
Product level	L1
Product type	Single Look Complex (SLC)
Path	167
Frame	475
Date	27 April 2015 (03:50:54 UTC)
Instrument	SAR-C
Mode	Interferometric Wide swath (IW)
Satellite	Sentinel-1
Absolute Orbit number	5664
Pass direction	DECENDING
Polarization	VV + VH
Product level	L1
Product type	Single Look Complex (SLC)
Path	167
Frame	475

(v11) was used. The latest is a hybrid product based on SRTM and ASTER GDEM data fused by a weighted averaging approach [41].

Step 3: Formation of a lookup table between DEM and SAR imagery. In this step, a lookup table for SLC co-registration, considering terrain heights is created. The data are filtered with adaptive data filtering.

Step 4: Generation of a differential interferogram using the DEM height along with the coregistration with the DEM. At this step, a simulation of the unwrapped interferometric phase using the EU-DEM height is created, and deformation rate using orbit state vectors.

Step 5: Removal of the flat earth phase.

Step 6: Removal of the topographic phase.

Step 7: Refinement of the slave image with the master image due to offsets. A check for convergence is performed using the azimuth offset as a limit (less than 0.02 pixels).

Step 8: Resampling of the slave image to match the master one.

Step 9: Creation of the final interferogram.

Step 10: Unwrapping the phase using the minimum cost flow (MCF) algorithm. MCF algorithm permits a global automatic optimization robust phase unwrapping taking into consideration disconnected areas of high coherence.

Step 11: Geocoding the results and completion of generating the output products.

The ascending and descending pairs of Sentinel-1images are different processing products within the HyP3 platform. The processing time on this cloud platform was estimated to be 1 h for each pair of images, providing the following end-products.

1) Wrapped interferogram (in PNG image and KMZ file).
2) Unwrapped interferogram (in GeoTIFF, PNG images, and KMZ file).
3) LOS displacement map (in GeoTIFF format).
4) Vertical displacement map (in GeoTIFF format).
5) Coherence map (in GeoTIFF format).
6) Amplitude image (in GeoTIFF format).

The following section presents the overall results for both orbits (ascending and descending).

V. RESULTS

The first result generated from the InSAR processing is the wrapped interferogram. Wrapped interferogram indicates phase fringes corresponding to half the radar wavelength [42].

The phase difference map, i.e., the interferometric phase at each SAR image pixel, depends—if we exclude all other factors, see also next section—on the difference in the travel paths from the Sentinel-1 sensor to a specific point (pixel) during the acquisition of each image.

The wrapped interferogram is useful for visualization purposes, as it shows deformation in multiples of half of the sensor wavelength. Interferometric fringes represent a full 2π cycle of phase change. Fringes appear on an interferogram as cycles of colors, with each cycle representing relative range difference of half a sensor's wavelength, in the LOS direction from the sensor [43], [44].

Fig. 3 shows these fringes for both ascending (see Fig. 3, top) and descending (see Fig. 3, bottom) orbits. The location of the epicenter is also shown in Fig. 3 with a red dot. Each fringe corresponds to change in range of $\lambda/2$, where λ is the radar wavelength ($\sim$5.54 cm for the Sentinel-1 satellite). The closer the fringes are together, the higher the deformation on the ground. As evident, the descending and the ascending orbits tend to give different results, as this will also be discussed in the next section. Examining the descending orbit result (deformation fringes at Fig. 3, bottom), it shows that no significant deformation has

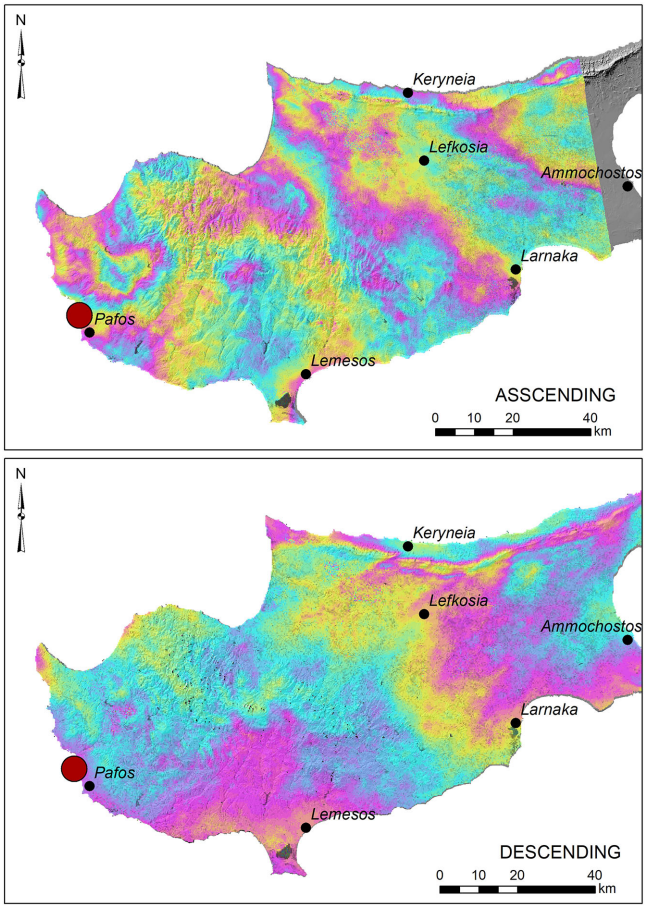

Fig. 3. Deformation fringes related to the earthquake of 15th of April 2015, as derived from the Sentinel-1 SAR images in ascending orbit (top) and descending orbit (bottom). The location of the earthquake is shown with the red dot.

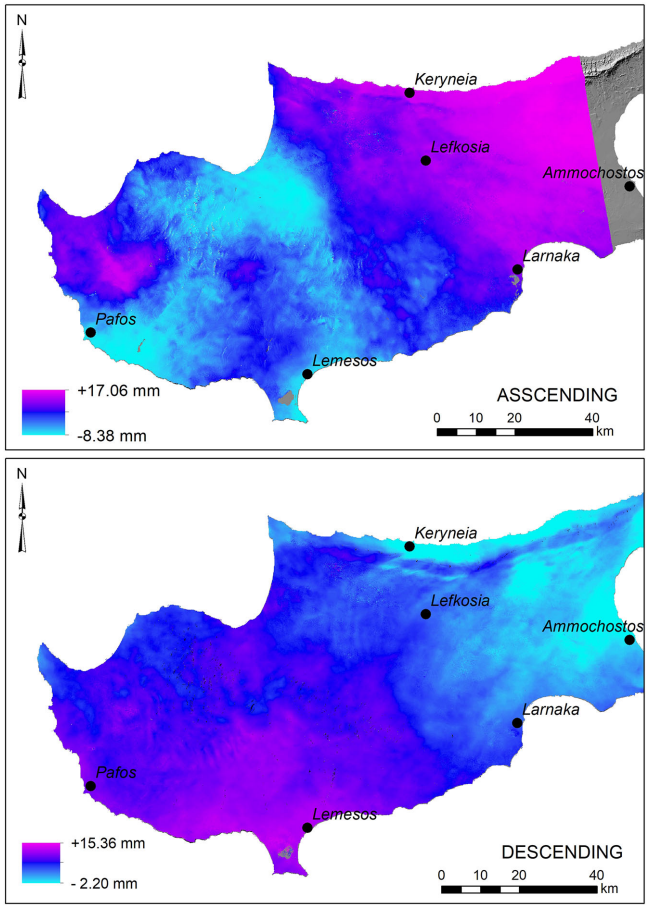

Fig. 4. Unwrapped interferogram as derived from the Sentinel-1 SAR images in ascending orbit (top) and descending orbit (bottom).

taken place during this period (i.e., 15th April–27th April 2015, Sentinel-1 image, Table II). In contrast, the ascending orbit (see Fig. 3, top), reveals a pattern near Paphos town, on the south and south of the earthquake event.

Once the wrapped interferogram was produced, then the so-called, unwrapped interferogram that converts the wrapped 2-π scale into a continuous scale (of multiples of pi) is produced.

Phase unwrapping process was based on the MCF and triangulation method (see more in [46]). Fig. 4 shows the unwrapped values of the area under investigation, corresponding to the change in the distance along the LOS of the sensor. Fig. 4 (top) shows the results from the ascending orbit, while Fig. 4 (bottom) the results from the descending one. Values greater than zero (positive) indicate movement away from the sensor (subsidence) (purple color in Fig. 4), while negative values (blue color in Fig. 4) indicate movement toward the sensor (uplift).

Finally, a vertical displacement map was generated from the platform under the assumption that the interferometric phase is related to topography only (see also section below). Values are in meters, with positive values indicating uplift and negative values indicating subsidence. To produce the displacement, map (1) was used. It should be mentioned that these displacement values are relative values.

$$\text{Vertical displacement}_{(\text{mm})} = (\varphi\text{unwrapped} \times \lambda\,(\text{mm}))/ 4\pi \times \cos\theta_{\text{incident}} \quad (1)$$

The results are shown in Fig. 5 for the ascending orbit (top) and descending orbit (bottom).

VI. Coherence and Cross Comparison

While the previous findings were derived from the HyP3 platform as ready products, it is important to examine their accuracy and consistency. A first attempt can be made for both products (i.e., ascending and descending orbits) through their coherence maps, that indicate the level of accuracy of the images used in each pair.

The degree of coherence is defined as the magnitude of the normalized interferogram g, defined as the normalized complex correlation coefficient of the complex backscatter intensities s_1 and s_2 [45]. Coherence is estimated using (2).

$$\gamma = \left| \frac{\langle S_2 S_1 * \rangle}{\sqrt{\langle S_1 S_1 * \rangle \langle S_2 S_2 * \rangle}} \right| . \quad (2)$$

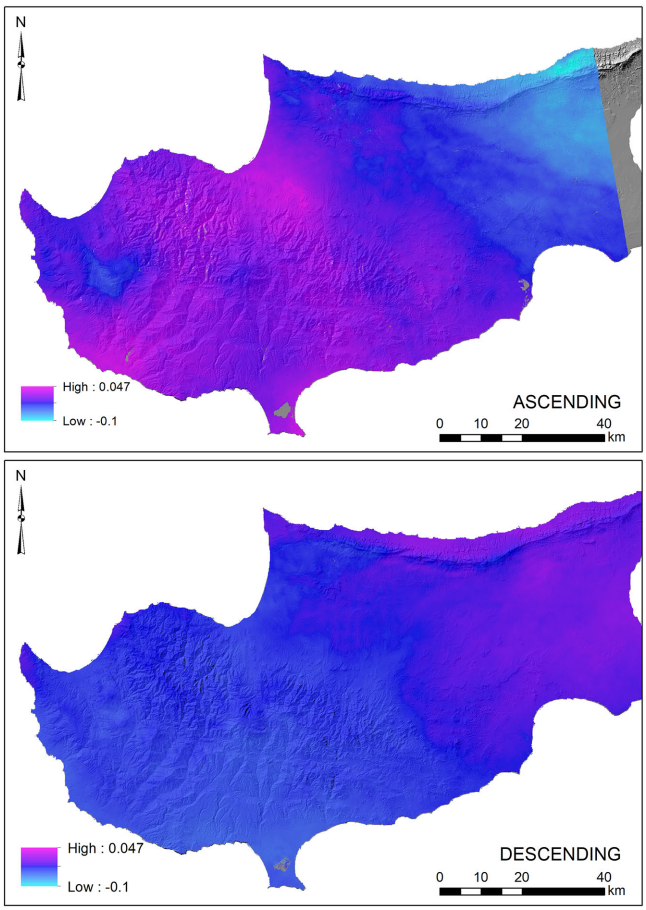

Fig. 5. Vertical displacement map as derived from the Sentinel-1 SAR images in ascending orbit (top) and descending orbit (bottom).

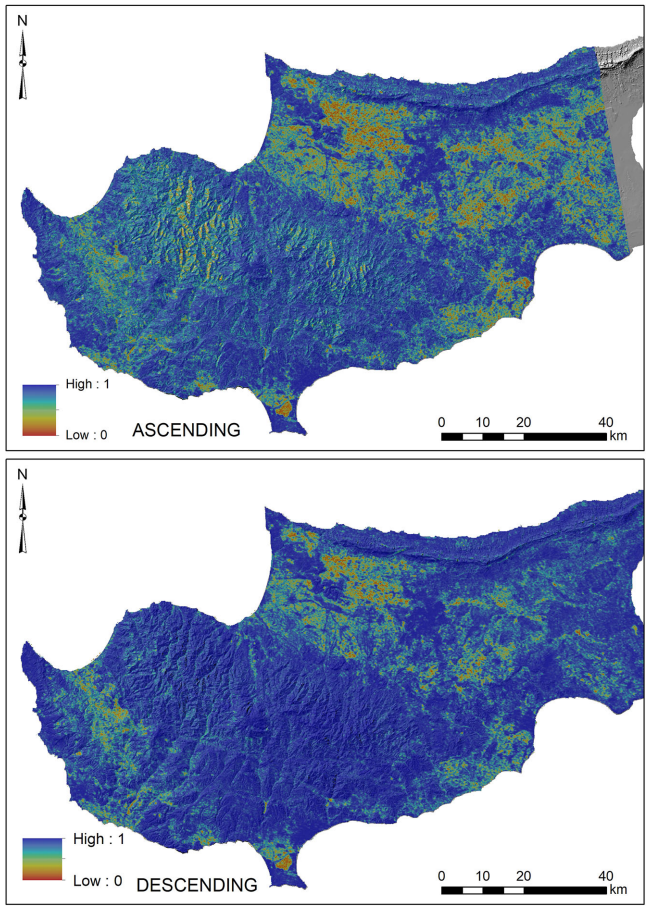

Fig. 6. Coherence map as derived from the Sentinel-1 SAR images in ascending orbit (top) and descending orbit (bottom).

The coherence map of the interferogram is a crucial indicator showing the reliability of the interferometric phase [46]. Coherence values range from 0 to 1; the larger the number, the higher the coherence. The coherence map for both ascending and descending orbits are shown in Fig. 6 (top and bottom, respectively). Areas highlighted with red color indicate regions with low coherence. Therefore, the vertical displacements and wrapped interferogram are influenced by noise, while blue color indicates areas with less noise, and therefore, the results are more accurate. As it is evident, the coherence map is different for both orbits. A threshold of around the 0.60 coherence value is usually used to exclude areas with noise [16].

Noise can influence the results of the InSAR analysis. In general, the interferometric phase ($\Delta\varphi$) is impacted by four parameters as these are described in the following equation.

1) Topographic distortions arising from slightly different viewing angles of the two-satellite passes (t) (these distortions have been taken into consideration for the vertical displacement maps, Fig. 5).
2) The atmospheric effects (α).
3) Range displacement of the radar target (ΔR) (for moving objects).
4) Other noise such as decorrelation effects (as these are also indicated from the coherence maps, Fig. 6).

The interferometric phase ($\Delta\varphi$) is estimated using (3)

$$\Delta\varphi = \frac{4\pi}{\lambda}\Delta R + \alpha + t + \text{noise}. \tag{3}$$

Therefore, differences between the two pairs of images, in ascending and descending orbits, can be explained considering the variables affecting the coherence level, which differs due to the atmospheric effects, as the images were taken from different angles and on different dates.

A common way to examine the ascending and descending deformation analysis products is a cross-comparison between them [47]. A cross-comparison of the InSAR measurements can quantitatively inform us about the consistency of measurements between these two products. Any differences could be due to the noise, as earlier described, as well as due to georeferencing uncertainty, seasonal biases and different temporal coverage. For the needs of this cross comparison, more than 8500 random points were used. These points are randomly scattered over the area of interest. For these points, the vertical displacement (corrected with the cosine of the incidence angles), for both ascending and descending Sentinel-1 images, was calculated.

The cross-comparison result of both orbits is shown in Fig. 7. Similar findings were also observed after the elimination of points with coherence value less than 0.60 (not shown here). The low correlation value between these two datasets should be not

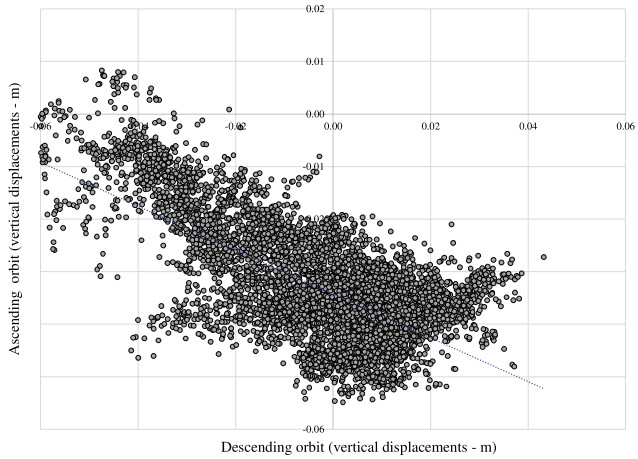

Fig. 7: Quantitative comparison of the LOS displacement rates between ascending and descending orbits. Offset from zero is related to local viewing angles' differences, but also to other noise.

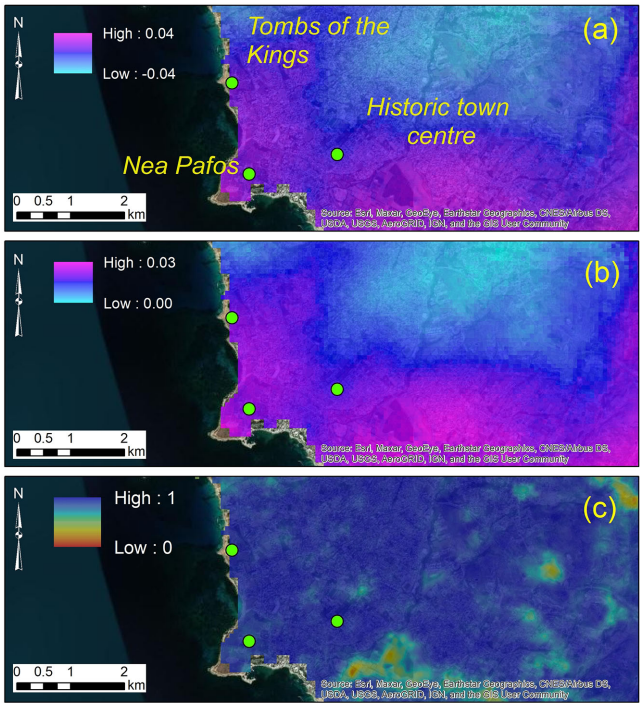

Fig. 8: (a) Unwrapped interferogram. (b) Vertical displacements. (c) Coherence map, enveloping important archaeological sites of the area.

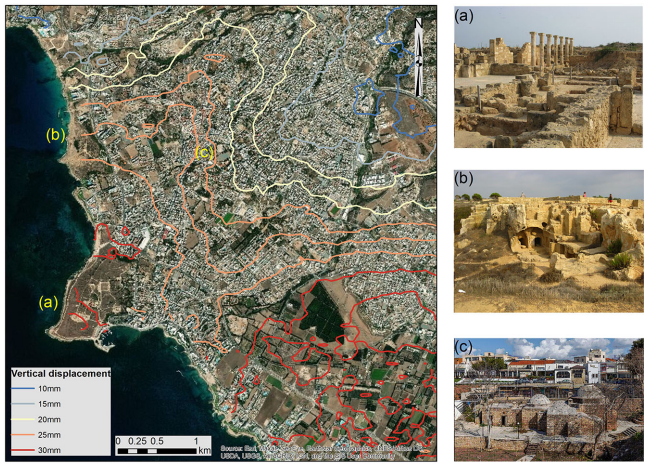

Fig. 9: Quantification of vertical displacements based on Fig. 8(b). Area (a) indicates the archaeological site of "Nea Paphos," area, (b) the archaeological site of the "Tombs of the Kings", and area (c) the historic center of Paphos town.

TABLE IV
UNWRAPPED INTERFEROGRAM (UNIT: METERS)

Unwrapped interferogram (unit: meters)		
Nea Paphos	0.019	0.023
Tombs of the Kings	0.017	0.018
Historic Centre	0.014	0.018
Vertical displacement (unit: meters)		
Nea Paphos	0.024	0.028
Tombs of the Kings	0.023	0.024
Historic Centre	0.012	0.014
Coherence map (unit: %)		
Nea Paphos	0.80	0.94
Tombs of the Kings	0.79	0.85
Historic Centre	0.93	0.96

only restricted to the different viewing angles of the ascending and descending orbits of the sensors, but also to other noise (see above).

VII. DEFORMATION ANALYSIS IN THE VICINITY OF ARCHAEOLOGICAL SITES

The results obtained from the ascending orbit were further analyzed and exploited to understand the possible impacts of the seismic event on archaeological sites. Significantly, the area of the earthquake's epicenter coincides with important archaeological sites and monuments on the western part of Cyprus, in Paphos town. At this area are located the archaeological park of Nea Paphos (the capital of Cyprus during the Hellenistic and Roman periods) [48], the ancient necropolis "Tombs of the Kings" [49], both listed in the UNESCO World Heritage monuments catalogue, as well as other heritage sites and historic buildings (see Fig. 8).

The InSAR analysis resulted in small ground displacements in the specific area, both from the images taken in ascending orbit and the seismic network (see *Akamas* station). Fig. 8(a) indicates the results from the unwrapped interferogram, while Fig. 8(b) evidences the vertical displacement results. Finally, Fig. 8(c) shows the coherence values based on the pair of Sentinel-1 images used in the ascending orbit (see Table II). The images used for Fig. 8(a)–(c), were enhanced using a standard deviation nonlinear histogram enhancement to highlight small displacements in the area. Areas with low coherence values (less

than 70%, Fig. 8(c) were excluded from the analysis (i.e., areas highlighted with red in Fig. 8(c).

The map of Fig. 9 clearly highlights the quantification of the vertical displacements based on Fig. 8(b) and following the contours of the examined area. The most significant relative ground displacements are precisely recorded within the archaeological sites, accommodating amongst others, freestanding columns [i.e., Fig. 9(a)].

In the light of the above, it becomes evident that relative displacements have occurred in the areas of the UNESCO Heritage sites. The displacements retrieved from the current interferometric analysis are also supported by the findings of a similar study, emanated from the same seismic event [16].

Table IV reproduces the quantification of the displacements detected. The range of values for (a)–(c) areas of Fig. 8 are given in meters [for Fig. 8(a) and 8(b)] and absolute unit [for Fig. 8(c)].

VIII. Conclusion

This study showcased the existing capacities of big-data cloud platforms to support radar processing chains, such as those of InSAR analysis using Sentinel-1 data. These platforms can provide ARD for heritage management, after a sudden natural hazard in a short time.

The earthquake event that emanated this study is the biggest reported in Cyprus, since the launch of the Sentinel-1 sensors. The selection of this type of sensor was made upon its free and open access policy based on which the ESA permits researchers to work with and elaborate on this type of data. In addition, the access to the HyP3 platform, even in beta version, fulfills a more general scope, that of monitoring large sites in a systematic way, rapidly and shortly before or after seismic events. Monitoring purposes aside, the presented pipeline is of importance regarding the detection of possible damages on monuments, the quantification of the damage and consequently the prioritization of physical intervention for conservation purposes, the development of strategic preservation planning (i.e., accumulative displacements in a specific area/monument, should be given priority).

The results of the interferometric analysis are enhanced by the ground seismic network station of the Cyprus Geological Survey Department. Especially for the area of *Akamas,* where a significant peak ground displacement HHE (vertical movements) was recorded both by ground and satellite data. This alignment further validates the scientific path showcased in the present study.

Another key finding of this study is that the datasets used were processed in less than 1-h for each orbit, thus significantly minimizing the computational time compared to traditional desktop analysis. This observation underlines the continuous improvement of the processing time for ARD.

The use of ARD products produced through the HyP3 platform, are key inputs for heritage management, as they can provide displacement information over large areas, in a very short time. Their use is expected to grow in the near future as the big-data technology is growing.

However, as in almost all earth observation processing chains, these results require ground verifications and calibrations. Therefore the interferometric analysis here presented, also merits the same approach for a comprehensive and integrated outcome, primarily due to the ground sensitivity of the specific research field, namely *in situ* archaeological remains.

Acknowledgment

The authors would like to thank Alaska Satellite Facility (ASF) for providing access to the Hybrid Pluggable Processing Pipeline (HyP3), beta version. The data were processed through the ASF DAAC 2020 using GAMMA software. The work contains modified Copernicus Sentinel data 2015, processed by ESA. They would like to thank Cyprus Geological Survey Department for the seismic data, accessible through their official website. And also would like to thank the Eratosthenes Research Centre of the Cyprus University of Technology for its support.

References

[1] F. Chen, R. Lasaponara, and N. Masini, "An overview of satellite synthetic aperture radar remote sensing in archaeology: From site detection to monitoring," *J. Cultural Heritage*, vol. 23, no. Supplement, pp. 5–11, 2017.

[2] R. Lasaponara and N. Masini, "Satellite synthetic aperture radar in archaeology and cultural landscape: An overview," *Archaeol. Prospection*, vol. 20, pp. 71–78, 2013.

[3] N. Dore, J. Patruno, E. Pottier, and M. Crespi, "New research in polarimetric SAR technique for archaeological purposes using ALOS PALSAR data," *Archaeol. Prospection*, vol. 20, pp. 79–87, 2013.

[4] M. Noviello, M. Ciminale, and V. D. Pasquale, "Combined application of pansharpening and enhancement methods to improve archaeological cropmak visibility and identification in QuickBird imagery: Two case studies from Apulia, Southern Italy," *J. Archaeol. Sci.*, vol. 40, pp. 3604–3613, 2013

[5] D. Tapete and F. Cigna, "Trends and perspectives of spaceborne SAR remote sensing for archaeological landscape and cultural heritage applications," *J. Archaeol. Sci. Rep.*, vol. 14, pp. 716–726, 2017

[6] D. Tapete, F. Cigna, and D. N. M. Donoghue, "Looting marks" in spaceborne SAR imagery: Measuring rates of archaeological looting in Apamea (Syria) with TerraSAR-X Staring Spotlight," *Remote Sens. Environ.*, vol. 178, pp. 42–58. 2016.

[7] A. Agapiou, "Detecting looting activity through earth observation multitemporal analysis over the archaeological site of Apamea (Syria) during 2011–2012," *J. Comput. Appl. Archaeol.*, vol. 3, no. 1, pp. 219–237, 2020.

[8] D. Tapete and F. Cigna, "Poorly known 2018 floods in Bosra UNESCO site and Sergiopolis in Syria unveiled from space using Sentinel-1/2 and COSMO-SkyMed," *Sci Rep.*, vol. 10, 2020, Art. no. 12307.

[9] L. Luo *et al.*, "Airborne and spaceborne remote sensing for archaeological and cultural heritage applications: A review of the century (1907–2017)," *Remote Sens. Environ.*, vol. 232, 2019, Art. no. 111280.

[10] A. Agapiou and L. Lysandrou, "Remote sensing archaeology: Tracking and mapping evolution in scientific literature from 1999–2015," *J. Archaeol. Sci. Rep.*, vol. 4, pp. 192–200, 2015.

[11] P. Milillo, B. Riel, B. Minchew, S. H. Yun, M. Simons and P. Lundgren, "On the synergistic use of SAR constellations' data exploitation for earth science and natural hazard response," *IEEE J. Sel. Topics Appl. Earth Observ. Remote Sens.*, vol. 9, no. 3, pp. 1095–1100, Mar. 2016.

[12] S. H. Yun *et al.*, "Rapid damage mapping for the 2015 M w 7.8 Gorkha earthquake using synthetic aperture radar data from COSMO–SkyMed and ALOS-2 Satellites," *Seismol. Res. Lett.*, vol. 86, no. 6, pp. 1549–1556, 2015.

[13] Y. Lou, D. Clark, P. Marks, R. J. Muellerschoen, and C. C. Wang, "Onboard radar processor development for rapid response to natural hazards," *IEEE J. Sel. Topics Appl. Earth Observ. Remote Sens.*, vol. 9, no. 6, pp. 2770–2776, Jun. 2016.

[14] L. Bingquan, L. Yongsheng, J. Z. S. Wenliang, and S. Wenhao, "Conjugate ruptures and seismotectonic implications of the 2019 Mindanao earthquake sequence inferred from Sentinel-1 InSAR data," *Int. J. Appl. Earth Observ. Geoinf.*, vol. 90, 2020, Art. no. 102127.

[15] S. L. Ullo *et al.*, "Application of DInSAR technique to high coherence sentinel-1 images for dam monitoring and result validation through in situ measurements," *IEEE J. Sel. Topics Appl. Earth Observ. Remote Sens.*, vol. 12, no. 3, pp. 875–890, Mar. 2019.

[16] M. Tzouvaras, D. Kouhartsiouk, A. Agapiou, C. Danezis, and D. G. Hadjimitsis, "The use of Sentinel-1 synthetic aperture radar (SAR) images and open-source software for cultural heritage: An example from Paphos area in Cyprus for mapping landscape changes after a 5.6 magnitude earthquake," *Remote Sens.*, vol. 11, 2019, Art. no. 1766.
[17] F. Cigna, R. Lasaponara, N. Masini, P. Milillo, and D. Tapete, "Persistent scatterer interferometry processing of cosmo-skymed stripmap Himage time series to depict deformation of the historic centre of Rome, Italy," *Remote Sens.*, vol. 6, pp. 12593–12618, 2014.
[18] D. Tapete and F. Cigna, "InSAR data for geohazard assessment in UNESCO World Heritage sites: State-of-the-art and perspectives in the Copernicus era," *Int. J. Appl. Earth Observ. Geoinf.*, vol. 63, pp. 24–32, 2017.
[19] D. H. T. Minh, R. Hanssen, and F. Rocca, "Radar Interferometry: 20 Years of development in time series techniques and future perspectives," *Remote Sens*., vol. 12, 2020, Art. no. 1364.
[20] M. E. Kamali, A. Abuelgasim, I. Papoutsis, C. Loupasakis, and C. Kontoes, "A reasoned bibliography on SAR interferometry applications and outlook on big interferometric data processing," *Remote Sens. Appl., Soc. Environ.*, vol. 19, 2020, Art. no. 100358.
[21] M. Crosetto *et al.*, "The evolution of wide-area dinsar: From regional and national services to the European ground motion service," *Remote Sens*., vol. 12, 2020, Art. no. 2043.
[22] Y. Morishita, M. Lazecky, T. J. Wright, J. R. Weiss, J. R. Elliott, and A. Hooper, "LiCSBAS: An open-source INSAR time series analysis package integrated with the LiCSAR Automated Sentinel-1 InSAR Processor," *Remote Sens.*, vol. 12, 2020, Art. no. 424.
[23] C. Yang, Q. Huang, Z. Li, K. Liu, and F. Hu, "Big data and cloud computing: Innovation opportunities and challenges," *Int. J. Digit. Earth*, vol. 10, no. 1, pp. 13–53, 2017.
[24] A. Agapiou, "Remote sensing heritage in a petabyte-scale: Satellite data and heritage Earth Engine© applications," *Int. J. Digit. Earth*, vol. 10, no. 1, pp. 85–102, 2017.
[25] C. Xu, X. Du, Z. Yan, and X. Fan, "ScienceEarth: A big data platform for remote sensing data processing," *Remote Sens.*, vol. 12, 2020, Art. no. 607.
[26] A. Agapiou, V. Lysandrou, and D.G. Hadjimitsis, "Earth observation contribution to cultural heritage disaster risk management: Case study of eastern mediterranean open air archaeological monuments and sites," *Remote Sens*., vol. 12, 2020, Art. no. 1330.
[27] Google Earth Engine (GEE). Accessed: Sep. 18, 2020. [Online]. Available: https://earthengine.google.com
[28] A. H. Orengo *et al.*, "Automated detection of archaeological mounds using machine-learning classification of ultisensory and multitemporal satellite data," *Proc. Nat. Acad. Sci.*, vol. 117, no. 31, pp. 18240–18250, Aug. 2020.
[29] K. Hogenson, S.A. Arko, B. Buechler, R. Hogenson, J. Herrmann, A. Geiger, A., "Hybrid pluggable processing pipeline (HyP3): A cloud-based infrastructure for generic processing of SAR data," *presented at 2016 AGU Fall Meeting*, San Francisco, CA, 12-16 Dec. 2016.
[30] Alaska Satellite Facility (ASF). Accessed: Aug. 13, 2020. [Online]. Available: https://asf.alaska.edu.
[31] A. P. Nicolau, A. Flores-Anderson, R. Griffin, K. Herndon, and F. J. Meyer, "Assessing SAR C-band data to effectively distinguish modified land uses in a heavily disturbed Amazon forest," *Int. J. Appl. Earth Observ. Geoinf.*, vol. 94, 2021, Art. no. 102214.
[32] About HyP3. Accessed: Aug. 13, 2020. [Online]. Available: https://hyp3.asf.alaska.edu/about
[33] S.A. Arko, R. Hogenson, A. Geiger, J. Herrmann, B. Buechler, and K. Hogenson, "Sentinel-1 archive and processing in the cloud using the hybrid pluggable processing pipeline (HyP3) at the ASF DAAC," presented at the 2016 American Geophysical Union, Fall Meeting, 2016.
[34] Sentinel Toolbox. Accessed: Aug. 13, 2020. [Online]. Available: https://sentinel.esa.int/web/sentinel/toolboxes
[35] Gamma software. Accessed: Aug. 13, 2020. [Online]. Available: https://www.gamma-rs.ch
[36] N. Kyriakides, V. Lysandrou, A. Agapiou, P. Illampas, and E. Charalambous, "Correlating damage condition with historical seismic activity in underground sepulchral monuments of Cyprus," *J. Archaeol. Sci. Rep.*, vol. 14, pp. 734–741, 2017.
[37] G. Constantinou and I. Panagides, *Kypros kai Geologia*, (in Greek), Nicosia, Cyprus, 2013.
[38] Current Seismicity Maps from the Geological Department of Cyprus. Accessed: Aug. 13, 2020. [Online]. Available: http://81.4.135.34:8080/en/events/map
[39] A. Gaber, N. Darwish, and M. Koch, "Minimizing the residual topography effect on interferograms to improve dinsar results: Estimating land subsidence in port-said city," Egypt. *Remote Sens.,* vol. 9, 2017, Art. no. 752.
[40] ASF HyP3 team, "Sentinel-1 InSAR GAMMA clarrification," private communication, Sep. 2020.
[41] EU-DEM. Accessed: Sep. 22, 2010. [Online]. Available: https://www.eea.europa.eu/data-and-maps/data/copernicus-land-monitoring-service-eu-dem
[42] S. Gudmundsson, J. M. Carstensen, and F. Sigmundsson, "Unwrapping ground displacement signals in satellite radar interferograms with aid of GPS data and MRF regularization," *IEEE Trans. Geosci. Remote Sens.*, vol. 40, no. 8, pp. 1743–1754, Aug. 2002.
[43] D. Massonnet and K. L. Feigl, "Radar interferometry and its applications to changes in the earth's surface," *Rev. Geophys.*, vol. 36, pp. 441–500, Nov. 1998.
[44] R. Bamler and P. Hartl, "Synthetic aperture radar interferometry," *Inverse Problems*, vol. 14, pp. R1–R54, 1998.
[45] C. L. Werner, U. Wegmüller, and T. Strozzi, "Processing strategies for phase unwrapping for InSar applications," Accessed: Aug. 13, 2020. [Online]. Available: https://www.gamma-rs.ch/uploads/media/2002-4_PhaseUnwrapping.pdf
[46] X. Sun, A. Zimmer, S. Mukherjee, N. K. Kottayil, P. Ghuman, and I. Cheng, "DeepInSAR—A deep learning framework for SAR interferometric phase restoration and coherence estimation," *Remote Sens*, vol. 12, 2020, Art. no. 2340.
[47] G. Aslan, Z. Cakir, C. Lasserre, F. Renard, "Investigating Subsidence in the Bursa Plain, Turkey, using ascending and descending Sentinel-1 satellite data," *Remote Sens*., vol. 11, 2019, Art. no. 85.
[48] J. Młynarczyk, *Nea Paphos in the Hellenistic Period*, Éditions Géologiques, Varsovie, Poland, 1990.
[49] M. Hadjisavva, *The Tombs of the Kings*. Nicosia, Poland, 1982.

Athos Agapiou was born in Limassol, Cyprus, in 1980. He received the Diploma and M.Sc. degrees in surveying engineering and geoinformatics from the National Technical University of Athens, Athens, Greece, in 2007, the M.A. degree in archaeology from the University of Cyprus, Nicosia, Cyprus, in 2010, and the Ph.D. degree in remote sensing archaeology from the Cyprus University of Technology, Limassol, Cyprus, in 2013.

Since 2008, he has been working as a Researcher with the Cyprus University of Technology. He has authored more than 70 articles in scientific journals and more than 200 papers in conference proceedings. He has been actively involved in several research projects, funded from various sources. His research interests include the analysis of earth observation satellite data, blended with archive aerial and other information, as well as ground prospection investigations over archaeolandscapes.

Vasiliki Lysandrou was born in Nicosia, Cyprus, in 1980. She received the Diploma in archaeology from the Aristotelian University of Thessaloniki, Thessaloniki, Greece, in 2003, athe Diploma di Lingua e Cultura Italiana di Livello Superiore from Scuola Leonardo Da Vinci Roma, Roma, Italy, in 2004, the Diploma di Specializzazione in Restoration of Monuments from the Architectural School Valle Giulia of the University of Rome La Sapienza, Roma, Italy, in 2007, and the Ph.D. degree in mediterranean archaeology from the University of Cyprus, Nicosia, Cyprus, in 2014.

Since 2014, she has been working as a Researcher with the Cyprus University of Technology. She authored several articles in scientific journals and conference proceedings, and she was actively involved in several research projects. Her research interests include the study, survey, and analysis of standing archaeological remains and monuments; aerial archaeology; remote sensing (satellite, middle range, and terrestrial) intended for archaeological research; funerary architecture, and archaeology of death.